Journal of Zhejiang University-SCIENCE A (Applied Physics & Engineering) 2022 23(6):421-442
www.jzus.zju.edu.cn; www.springer.com/journal/11582
E-mail: jzus_a@zju.edu.cn

Research Article

https://doi.org/10.1631/jzus.A2100369

Identification of ductile fracture model parameters for three ASTM structural steels using particle swarm optimization

Ya-zhi ZHU[1], Shi-ping HUANG[2,3]✉, Hao HONG[4]

[1]*Department of Structural Engineering, Tongji University, Shanghai 200092, China*
[2]*School of Civil Engineering and Transportation, South China University of Technology, Guangzhou 510640, China*
[3]*China-Singapore International Joint Research Institute, Guangzhou 510700, China*
[4]*Shanghai Municipal Engineering Design Institute (Group), Co., Ltd., Shanghai 200092, China*

Abstract: Accurate prediction of ductile fracture requires determining the material properties, including the parameters of the constitutive and ductile fracture model, which represent the true material response. Conventional calibration of material parameters often relies on a trial-and-error approach, in which the parameters are manually adjusted until the corresponding finite element model results in a response matching the experimental global response. The parameter estimates are often subjective. To address this issue, in this paper we treat the identification of material parameters as an optimization problem and introduce the particle swarm optimization (PSO) algorithm as the optimization approach. We provide material parameters of two uncoupled ductile fracture models—the Rice and Tracey void growth model (RT-VGM) and the micro-mechanical void growth model (MM-VGM), and a coupled model—the Gurson-Tvergaard-Needleman (GTN) model for ASTM A36, A572 Gr. 50, and A992 structural steels using an automated PSO method. By minimizing the difference between the experimental results and finite element simulations of the load-displacement curves for a set of tests of circumferentially notched tensile (CNT) bars, the calibration procedure automatically determines the parameters of the strain hardening law as well as the uncoupled models and the coupled GTN constitutive model. Validation studies show accurate prediction of the load-displacement response and ductile fracture initiation in V-notch specimens, and confirm the PSO algorithm as an effective and robust algorithm for seeking ductile fracture model parameters. PSO has excellent potential for identifying other fracture models (e.g., shear modified GTN) with many parameters that can give rise to more accurate predictions of ductile fracture. Limitations of the PSO algorithm and the current calibrated ductile fracture models are also discussed in this paper.

Key words: Parameter calibration; Void growth model (VGM); Gurson-Tvergaard-Needleman (GTN) model; A36 steel; A572 Gr. 50 steel; A992 steel; Particle swarm optimization (PSO)

1 Introduction

Ductile fracture is one of the most critical limit states in steel structures, and often governs the ultimate capacity of steel components and structures in many situations. Ductile tearing may result in complete failure of a structural component, and possibly the collapse of a building (Khandelwal and El-Tawil, 2007). With increasing interest in investigating the detailed response of steel structural systems, understanding and predicting ductile fracture is becoming of utmost significance. Modeling ductile fracture at the material level provides a basis for predicting ductile failure in steel structural components and systems.

Ductile fracture involves a complex process with high material and geometric nonlinearity. From the micro-mechanism standpoint, ductile fracture involves void nucleation, growth, and coalescence (Anderson, 2017). Stress and strain parameters, such as the equivalent plastic strain, ε_{eq}, and the stress triaxiality, T, (i.e., the ratio of hydrostatic stress σ_m to effective stress σ_e, $T=\sigma_m/\sigma_e$), play essential roles in void evolution (Benzerga and Leblond, 2010; Pineau et al., 2016). Many popular models have been developed to predict ductile fracture initiation in metals. Based on the understanding of micro-mechanisms, these models can

✉ Shi-ping HUANG, ctasihuang@scut.edu.cn
Ya-zhi ZHU, https://orcid.org/0000-0002-9783-2780
Shi-ping HUANG, https://orcid.org/0000-0002-0092-1753

Received Aug. 1, 2021; Revision accepted Jan. 12, 2022;
Crosschecked May 24, 2022

be generally categorized into two groups: uncoupled and coupled models. For uncoupled models, ductile fracture initiation is considered as the critical state without considering the influence of void evolution on the constitutive model (Anderson, 2017). The void growth model (VGM) proposed by Rice and Tracey (1969) (RT-VGM), along with its simplified and/or improved versions (Wen and Mahmoud, 2016; Yan and Zhao, 2018; Zhu and Engelhardt, 2018b; Kong and Yang, 2020) (e.g., the stress modified critical strain model (SMCS) (Kanvinde and Deierlein, 2006)), is a representative uncoupled model. In contrast, coupled models consider the degradation of effective stress due to presence and growth of voids. Typical coupled models are attributed to the micromechanics-based Gurson model (Gurson, 1977) and its extensions (Chu and Needleman, 1980; Tvergaard, 1981; Malcher et al., 2014). Gurson (1977) proposed a porosity-embedded yield potential function associated with the expression of void volumetric (porosity) evolution, which comprised the original form of the Gurson model. Tvergaard and Needleman (1984) improved the original Gurson model by considering the contribution of void coalescence to the sudden drop of load carrying capacity, which resulted in the development of the well-known Gurson-Tvergaard-Needleman (GTN) model.

Application of the popular fracture models requires calibration of the material constitutive parameters (strain hardening law) and toughness parameters. Fracture initiation and propagation are pertinent to the local continuum fields, which are sensitive to the constitutive model parameters. Thus, reliable modeling and prediction of these fracture events require knowledge of the constitutive relationship representing the true material behavior covering a full range of true stress-strain curves over large strain levels (larger than the strain at fracture initiation). Determination of the true stress-strain relationship is typically based on uniaxial tensile tests of circumferentially smooth round (SR) bars or coupon flat (CF) specimens. Due to the uniform distribution of the stress and deformation fields over the critical cross-section up to necking in SR bars or CF specimens, the measured load-displacement response (engineering stress-strain relation) from such tests can be analytically interpreted to back-calculate the true strain-true stress relationship at small strain levels (typically <0.2). Once necking is initiated in a tensile coupon test, deriving the true stress-strain relation from the measured engineering stress-strain becomes cumbersome. This is because both the stress and strain are highly non-uniform and complex in the necked region (uniaxial tension no longer exists in the necked region). To estimate the post-necking true stress-strain response, analytical solutions (e.g., Bridgman's correction (Bridgman, 1964)) and experimental-numerical iterative methods with a tensile SR bar or CF specimen are often employed. For the iterative methods, the true stress-strain curve in the finite element (FE) model is adjusted by trial-and-error until the simulated engineering stress-strain curve reasonably matches the experimentally measured engineering stress-strain curve (Defaisse et al., 2018; Neimitz et al., 2018). This method, however, has two main shortcomings. First, the FE model requires a very fine mesh in the necked region to mimic the actual necking shape up to fracture. The modeling associated with the repeated trial-and-error process often requires dozens of iterations, each of which involves several runs of FE modeling and manual adjustments to the true stress-strain curve. Thus, this method has high computational cost and low calibration efficacy. Second, the trial-and-error method for inferring the true stress-strain curve is subjective and highly dependent on human experience and expertise. The accuracy of the calibrated true stress-strain relation is usually evaluated through visual comparison of the simulated and measured engineering stress-strain curves, which may not be objective. All in all, the commonly used trial-and-error approach is of low efficacy, and the resulting material post-necking constitutive parameters include many uncertainties.

For calibrating uncoupled fracture models, tests on circumferentially notched tensile (CNT) bars are often used to achieve various levels of stress triaxiality that generate different fracture loci (Kanvinde and Deierlein, 2006). The local continuum stress and strain quantities in CNT bars are often computed based on the true stress-strain relations estimated from the SR bars or tensile coupon specimens. However, this true stress-strain relation often leads to the simulated CNT global response visibly deviating from the experimental test data. The primary reason is that the constitutive model specified for an SR/tensile coupon may not accurately describe the true material response in CNT bars. In this case, accurate estimates of the constitutive

model through CNT bars are preferred if the fracture model parameters are also identified using the same CNT bars. This, in turn, raises the difficulty of the estimation. Unlike the SR bar before necking, where the stress and deformation fields are uniform, there is no straightforward approach to calibrating the constitutive model in CNT bars. This is because the stress and strain fields in those specimens are non-uniform due to the high geometric nonlinearity induced by fabricated notches. Thus, it is impossible to determine the uncoupled fracture model parameters using only CNT bars by conventional approaches, which reduces the accuracy of the calibrated model parameters and the performance of the models in practical prediction applications.

For coupled damage models, parameter calibration is also challenging as the procedure involves identifying many parameters simultaneously (including constitutive model parameters). Conventional methods for determining the model parameters include experimental (microscopic and macroscopic) measurements and hybrid numerical-experimental methods (Pineau et al., 2016). Experimental measurements always require a large number of tests and are expensive. Hybrid methods are commonly implemented by fitting the simulated load-displacement curves to the experimental results. Hybrid methods are more popular as the procedures are relatively straightforward and have lower experimental costs than pure experimental measurements. However, like calibration of the uncoupled model parameters using SR and CNT bars, these hybrid numerical-experimental methods have shown deficiencies. They are considered less reliable because the procedures are essentially operated, relying on significant manual intervention. In general, the process of determining parameters of either the constitutive or the ductile fracture models can be recognized as an inverse problem. Rigorous approaches are likely required to address non-objectivity and improve the accuracy and efficiency in solving the inverse problem.

Thus, a computer-aided instead of trial-and-error approach is needed urgently for identifying the parameters of the constitutive and fracture models. Inverse analysis based upon nonlinear optimization techniques has shown great potential to address the parameter identification problem (Yoshida et al., 2003; Yun and Shang, 2011; Neimitz et al., 2018). The principle of this method is the application of an automated algorithm that incorporates numerical and experimental tools to find a set of material parameters that minimizes the difference between the test and simulated results. Previous studies have determined the efficiency and effectiveness of several optimization technologies in automatically calibrating constitutive model parameters, e.g., genetic algorithm (GA) (Pal et al., 1996) and particle swarm optimization (PSO) (Vaz Jr et al., 2016; Smith et al., 2017). Considerable efforts have also been made to identify the damage-coupled constitutive parameters. Mahnken (2002) used a gradient-based optimization strategy to determine the material parameters of many types of damage models. Abendroth and Kuna (2006) developed a neural network (NN) to establish the relation between damage parameters and the corresponding global load-displacement response calculated by finite element simulations. Once trained, the NN predicted the damage parameters using the available experimental measured load-displacement curves. Although optimization techniques have been extensively applied to numerous parameter identification problems, optimizing material parameters in uncoupled and coupled ductile fracture models for ASTM structural steels has not been well established. The PSO scheme has been shown to be the most effective for the specific problem of constitutive model calibration following a comparative evaluation of several popular methods, including random sampling (RS), gradient descent (GD), GA, and PSO (Smith et al., 2017). In the present study, we used PSO as the numerical method for optimization. With the assistance of the PSO search algorithm, many difficulties in calibrating uncoupled fracture and coupled damage models are expected to be resolved. For instance, the uncoupled fracture model and the strain hardening law can be directly determined based on CNT specimens without any need for manual intervention. The PSO algorithm also provides a potential numerical tool to identify coupled damage models with a significant number of parameters.

In this study, we focus on determining the ductile fracture model parameters for three kinds of structural steels widely used in the USA, i.e., ASTM A36, A572 Gr. 50, and A992 steels, using an automated PSO. First, we review previous experimental results concerning tensile tests on circumferentially notched bars. Also, we introduce three popular ductile fracture

models: the Rice and Tracey void growth model (RT-VGM), the micro-mechanical void growth model (MM-VGM), and the GTN model. A hybrid numerical-experimental approach using a PSO algorithm is first applied to calibrate the two uncoupled models and the strain hardening law. The same method with a different scheme is used to determine the GTN parameters. Validation studies of the calibrated models are performed using tests of V-notch specimens. The performance and further applications of the PSO algorithm in predicting the ductile fracture of steels are also discussed.

2 Ductile fracture models

There are many micromechanics-based and phenomenological ductile fracture models that are reasonably accurate in predicting fracture initiation. This section reviews three models, i.e., the RT-VGM, the MM-VGM, and the GTN model, which are popular in ductile fracture analysis of steel structures and materials. The RT-VGM and the MM-VGM are uncoupled models, while the GTN model represents a coupled model type.

2.1 Rice and Tracey void growth model

The RT-VGM was developed based on an isolated spherical void in an infinite matrix subjected to a remote stress field (McClintock, 1968; Rice and Tracey, 1969). The matrix was supposed to be either perfect elastic-plastic or linear strain hardening. The analytical solution for the growth rate of the void radius is expressed as:

$$\frac{\dot{\bar{R}}}{R_0}=\alpha\exp\left(\beta\frac{\sigma_{\mathrm{m}}}{\bar{\sigma}}\right)\dot{\varepsilon}_{\mathrm{eq}}, \tag{1}$$

where R_0 is the radius of the initial spherical void, $\dot{\bar{R}}=\left(\dot{\bar{R}}_1+\dot{\bar{R}}_2+\dot{\bar{R}}_3\right)/3$ is the average change rate of the radius in all three directions, and $\dot{\varepsilon}_{\mathrm{eq}}$ is the remote equivalent plastic strain rate imposed on the matrix. Without considering the stress degradation, the flow stress $\bar{\sigma}$ is equivalent to the effective stress σ_{e}. In the original RT-VGM, the parameter α was obtained as 0.283 and β was known as 1.5. By integrating Eq. (1), the current radius of the void is expressed as a function of stress triaxiality and the remote plastic strain field. According to Rice and Tracey (1969), the ductile fracture was assumed to initiate when the radius of the void exceeds a critical value over a characteristic length l^*. The criterion is explicitly expressed as

$$\mathrm{VGI}=\int_0^{\varepsilon_{\mathrm{eq}}}\exp(\beta T)\,\mathrm{d}\varepsilon_{\mathrm{eq}}\geqslant\mathrm{VGI}_{\mathrm{cr}},\quad R>l^*, \tag{2}$$

where VGI (void growth index) is to quantify the size of the void, and $\mathrm{VGI}_{\mathrm{cr}}$ is the critical void growth index. For the parameter β, Hancock and Brown (1983) emphasized that it was within 1.1 and 2.3 for British Steels 50D and 50D N.N, while Kiran and Khandelwal (2014a) suggested that 1.15 was appropriate for ASTM A992 steels. In this paper, the parameter β is considered a material property to be calibrated, rather than a constant. For the characteristic length l^*, we considered a length scale at fracture initiation, which implies that the condition in Eq. (2) must be satisfied over a certain length. In summary, there are three parameters for the VGM, i.e., the parameter β, the critical void growth index $\mathrm{VGI}_{\mathrm{cr}}$, and the characteristic length l^*, all of which must be calibrated either by experiments, FE simulations, or both.

2.2 Micro-mechanical void growth model (Kiran and Khandelwal model)

Kiran and Khandelwal (2013) developed the MM-VGM. Unlike the RT-VGM, the MM-VGM evaluates the initiation of ductile fracture based on the void volumetric quantity. By assuming a logarithmic form, the kernel function of MM-VGM is developed based on the results of computational cell simulations of void growth, given as:

$$\mathrm{MVGI}=\int_0^{\varepsilon_{\mathrm{eq}}}[\ln(T)+\lambda]\,\mathrm{d}\varepsilon_{\mathrm{eq}}\geqslant\mathrm{MVGI}_{\mathrm{cr}},\quad R>l^*, \tag{3}$$

where MVGI is related to the relative void volume ratio, λ is a material constant, and $\mathrm{MVGI}_{\mathrm{cr}}$ is the critical damage index, similar to the parameter $\mathrm{VGI}_{\mathrm{cr}}$ in the VGM. In the original version of MM-VGM, Kiran and Khandelwal (2013) suggested the parameter λ to be 1.47 for A992 steels. In the present study, it is considered as a material constant to be calibrated for different grades of steel. The characteristic length l^* has a physical representation similar to that in the VGM. Like RT-VGM, MM-VGM has three parameters to be calibrated.

Based on the RT-VGM, the MM-VGM states that ductile fracture initiates when the void volumetric parameter MVGI exceeds the critical value $\mathrm{MVGI}_{\mathrm{cr}}$ over the characteristic length l^*. The void volume fraction used to describe ductile fracture initiation may have advantages over the void radius parameter in the RT-VGM with regard to fracture prediction, particularly for fractures at relatively low triaxialities. As supported by Kiran and Khandelwal (2013), the relative void radius ratio used by the RT-VGM as the void growth indicator is doubtful for fractures under low triaxialities with a hardening material matrix. At intermediate and low triaxialities, the relative volume ratio is more sensitive than the relative void radius ratio to the sudden change of the void at the critical conditions (e.g., void coalescence and fracture initiation). Therefore, the void volumetric parameter can be a good indicator of abrupt void change (Pineau et al., 2016; Wen and Mahmoud, 2016; Zhu and Engelhardt, 2018b). However, this model is applicable only when $T>0$ and for ductile fracture, due to the void enlargement mechanism (Kiran and Khandelwal, 2013).

2.3 Gurson-Tvergaard-Needleman model

Based on a hollow sphere with a single void at the center, Gurson (1977) developed an expression for the void volumetric fraction (porosity), f, by using upper limit analysis. The surrounding matrix was assumed to follow J2 plasticity with isotropic strain hardening. The change rate of porosity is taken as:

$$\frac{\dot{f}}{f(1-f)}=\frac{3}{2}q\frac{\bar{\sigma}}{\sigma_{\mathrm{e}}}\sinh\left(\frac{3}{2}\frac{\sigma_{\mathrm{m}}}{\bar{\sigma}}\right)\dot{\varepsilon}_{\mathrm{eq}}, \tag{4}$$

where $\bar{\sigma}$ is the matrix flow stress, and q is a material constant. Analogous to the RT-VGM, the change rate of void size exponentially increases with the stress triaxiality. Comparison between Eqs. (1) and (4) indicates that the void volumetric fraction in the Gurson model considers the degradation of effective stress. In contrast, in the RT-VGM, the effect of damage is neglected, and the term $\bar{\sigma}/\sigma_{\mathrm{e}}$ is constant at 1. For a porous metal with dilute voids, Gurson (1977) proposed a yield condition as a function of the porosity, f, which was later modified by Tvergaard (1981) and Tvergaard and Needleman (1984) considering the effects of interaction between neighboring voids and void coalescence. The modified yield function is given as

$$\Phi=\frac{\sigma_{\mathrm{eq}}^2}{\bar{\sigma}^2}+2q_1f^*\cosh\left(\frac{3}{2}q_2\frac{\sigma_{\mathrm{m}}}{\bar{\sigma}}\right)-\left(1+q_3f^{*2}\right)\leqslant 0, \tag{5}$$

where the parameters q_i (i=1, 2, 3) were introduced by Tvergaard (1981), while in the original Gurson model $q_i=q=1$. Benzerga and Leblond (2010) supported the view that the additional parameters q_2 and q_3 were more likely to improve the predictive accuracy than representing the underlying physics of void growth. Some common adopted values of q_i (i=1, 2, 3) are attributed to q_1=1.15, 1.25, 1.5, q_2=1, and $q_3=q_1^2$.

The parameter f^* in Eq. (5) is the modified porosity, given as

$$f^*=\begin{cases} f, & f<f_{\mathrm{c}},\\ f_{\mathrm{c}}+\dfrac{\bar{f}_{\mathrm{F}}-f_{\mathrm{c}}}{f_{\mathrm{F}}-f_{\mathrm{c}}}\left(f-f_{\mathrm{c}}\right), & f_{\mathrm{c}}\leqslant f<f_{\mathrm{F}},\\ \bar{f}_{\mathrm{F}}, & f\geqslant f_{\mathrm{F}}, \end{cases} \tag{6}$$

where f_{c} is the critical porosity when the growth rate of porosity begins to accelerate until the failure porosity f_{F} is reached. Modification of the porosity incorporates the effects of micro-cracks and void coalescence in accelerating void growth for $f_{\mathrm{c}}\leqslant f<f_{\mathrm{F}}$. As the actual porosity f exceeds f_{F}, the porosity is assumed to be constant at $\bar{f}_{\mathrm{F}}=\left(q_1+\sqrt{q_1^2-q_3}\right)\Big/q_3$, and the material is considered to have completely lost its stress carrying capacity. Chu and Needleman (1980) suggested that the change rate of porosity comprised two terms due to void nucleation and growth of existing voids, taken as

$$\dot{f}=\dot{f}_{\mathrm{nuc}}+\dot{f}_{\mathrm{g}}, \tag{7}$$

where $\dot{f}_{\mathrm{nuc}}$ on the right-hand side describes the contribution of strain-controlled void nucleation, and is obtained using the relation $\dot{f}_{\mathrm{nuc}}=A(\bar{\varepsilon})\,\dot{\boldsymbol{\varepsilon}}_{\mathrm{eq}}$ ($\dot{\boldsymbol{\varepsilon}}_{\mathrm{eq}}$ is the plastic strain rate tensor). The coefficient $A(\bar{\varepsilon})$ is given as

$$A(\bar{\varepsilon})=\frac{f_{\mathrm{N}}}{s_{\mathrm{N}}\sqrt{2\pi}}\exp\left[-\frac{1}{2}\left(\frac{\bar{\varepsilon}-\varepsilon_{\mathrm{N}}}{s_{\mathrm{N}}}\right)^2\right]. \tag{8}$$

The coefficient $A(\bar{\varepsilon})$ is a function of strain, which follows a normal distribution with a mean nucleation strain ε_{N}, a standard deviation s_{N}, and a weighted

volume fraction of nucleating particles f_N. The second term $\dot{f}_g$ on the right-hand side of Eq. (7) represents the contribution of growth of the pre-existing voids and takes the form $\dot{f}_g = (1-f)\,\mathrm{tr}\boldsymbol{D}^p$, where $\boldsymbol{D}^p$ is the plastic part of the rate of deformation tensor.

The GTN model has nine parameters in total that need to be calibrated. These include: (1) q_i (i=1, 2, 3) in the yield potential function, (2) f_c and f_F for porosity modification, (3) ε_N, s_N, and f_N that are related to the void nucleation dominated growth of porosity, and (4) the initial porosity f_0.

3 Particle swarm optimization for parameter identification

The PSO method, originally proposed by Eberhart and Kennedy (1995), was inspired by the social behavior of a bird flock. The application of PSO search algorithms is favored in various fields for solving optimization problems owing to their simplicity, easy implementation, and robustness (Vaz Jr et al., 2016). As one of the most well-known metaheuristics, PSO enables researchers to search candidate solutions in large multi-dimensional spaces. A particle swarm (population) is first generated and located in the search-space in a uniformly distributed random manner. During each trial iteration, a velocity operator is assigned to each particle (candidate solution). The velocity and direction of the movement of each particle are guided by three factors: the previous velocity, the best-known position in the search-space, and the best-known position that any particle in this swarm has ever found. The three factors represent the inertia effect (moving following its previous direction), the individual cognition (best-known position in the search-space), and the social interaction of the bird swarm (best-known position in the swarm). As the historic best-known position of each particle is discovered, it would be collected and shared with the other particles in the swarm. The information package of the swarm is used to update the velocity and compute the new position of each particle. This allows the swarm to move towards the best solution. The iterative process is continued until either the optimal position is obtained, or the iteration criterion is met. The accepted best solution or the criterion is evaluated based upon the objective function, which is discussed as follows.

Given a swarm with n_p particles in an n-dimensional search-space (optimization of n parameters in the problem), the position of the particle i at iteration t is represented by a position vector $\boldsymbol{X}_i(t)=[x_{i,1}(t), x_{i,2}(t), \cdots, x_{i,n}(t)]^T$ (i=1, 2, $\cdots$, n_p) and the velocity is denoted by a vector $\boldsymbol{V}_i(t)=[v_{i,1}(t), v_{i,2}(t), \cdots, v_{i,n}(t)]^T$. At iteration t+1, the velocity and positive vectors are computed using Eqs. (9) and (10), respectively.

$$v_{i,j}(t+1) = wv_{i,j}(t) + \varphi_p u_p\left[p_{i,j} - x_{i,j}(t)\right] + \varphi_g u_g\left[p_{i,p} - x_{i,j}(t)\right], \quad j=1, 2, \cdots, n, \tag{9}$$

$$x_{i,j}(t+1) = x_{i,j}(t) + v_{i,j}(t+1), \tag{10}$$

where w is the inertial weight, and φ_p and φ_g are two positive constants. The parameter φ_p weighs the importance of each particle's personal best position, whereas φ_g represents the contribution of the global best. The parameters $p_{i,j}$ and $p_{i,p}$ denote the best particle position and the best position across all particles, respectively. The parameters u_p and u_g are two random-value parameters that lie within the range of [0, 1].

As suggested by Smith et al. (2017), for the specific problem of the calibration of cyclic constitutive models, the inertia weight factor w can be initially given a value of 0.55. This decreases linearly throughout the iterative process to a final value equal to half of the initial value (0.275), thus increasing the chance of finding the best solution. Smith et al. (2017) also investigated the effects of the two constants φ_p and φ_g on the calibration efficiency, and found that both were equal to 1.5 and provided good performance in terms of the calibration success rate. As the present study focused on a problem similar to that of Smith et al. (2017), the parameters of inertia weight w, and the two constants φ_p and φ_g, were given the same values as those suggested by Smith et al. (2017). The evaluation of the population size (number of particles) by Smith et al. (2017) showed that the population size (number of particles) had little effect on the success rate. However, as agreed by Vaz Jr et al. (2016), an appropriate number of particles was important for both the robustness and the rate of convergence of the PSO analysis. The recommended value of n_p is 3–6 times the dimension of the search-space, indicating that n_p ranges from 3n to 6n (Vaz Jr et al., 2016; Smith et al., 2017).

The process of PSO is started by initializing the particle's position with a uniformly distributed random

vector x_{ij}~U($\boldsymbol{b}^{\mathrm{lo}}$, $\boldsymbol{b}^{\mathrm{up}}$) (where $\boldsymbol{b}^{\mathrm{lo}}$ and $\boldsymbol{b}^{\mathrm{up}}$ represent the vectors of lower and upper boundaries, respectively, in the parametric space) and equating the particle's best known position to its initial position. In the following iterations, the velocity and position of each particle are updated using Eqs. (9) and (10). The fitness of each particle is evaluated using a pre-defined objective function $\varepsilon(Z)$ (where Z refers to the set of parameters in the search-space) that represents the error between the experimental and simulated global responses:

$$\varepsilon(Z)=\sum_{i\in S}\left|\frac{Q^i_{\mathrm{EXP}}-Q^i_{\mathrm{FEM}}}{Q^i_{\mathrm{EXP}}}\right|, \tag{11}$$

where S is the series of tests used in the calibration. The variables Q_{EXP} and Q_{FEM} denote the experimental and numerical quantities, respectively. Proposing an appropriate measure of error is crucial to the optimization process in terms of the constitutive relations or fracture models. Based upon the available measured force-deformation curves, the two quantities Q_{EXP} and Q_{FEM} and the measure of error are most likely the functions of force/deformation. Referring to the calibration of the constitutive models, Smith et al. (2017) recommended an integral term for each of the quantities, Q_{EXP} and Q_{FEM}, which are the integrals of force, F, with respect to the plastic displacement Δ_{p}, up to fracture initiation $\Delta^{\mathrm{f}}_{\mathrm{p}}$, and are expressed as:

$$\begin{cases} Q_{\mathrm{EXP}}=\displaystyle\int_0^{\Delta^{\mathrm{f}}_{\mathrm{p,\,EXP}}} F_{\mathrm{EXP}}\mathrm{d}\Delta_{\mathrm{p}}, \\ Q_{\mathrm{FEM}}=\displaystyle\int_0^{\Delta^{\mathrm{f}}_{\mathrm{p,\,EXP}}} F_{\mathrm{FEM}}\mathrm{d}\Delta_{\mathrm{p}}, \end{cases} \tag{12}$$

where $\Delta^{\mathrm{f}}_{\mathrm{p,\,EXP}}$ is the displacement to fracture initiation with respect to tests. Both terms on the right-hand side in Eq. (12) represent the dissipated energies. Therefore, the objective function in Eq. (11) becomes the normalized energy error term. In evaluating uncoupled fracture models, the global deformation at the initiation of fracture is commonly used to evaluate the predictive accuracy (Kanvinde and Deierlein, 2006; Wen and Mahmoud, 2016; Yan and Zhao, 2018; Zhu and Engelhardt, 2018b; Kong and Yang, 2020). Based on this, the two quantities Q_{EXP} and Q_{FEM} in the calibration of void growth-type models are given as:

$$\begin{cases} Q_{\mathrm{EXP}}=\Delta^{\mathrm{f}}_{\mathrm{p,\,EXP}}, \\ Q_{\mathrm{FEM}}=\Delta^{\mathrm{f}}_{\mathrm{p,\,FEM}}, \end{cases} \tag{13}$$

where $\Delta^{\mathrm{f}}_{\mathrm{p,\,FEM}}$ is the displacement to fracture initiation with respect to FE modeling. The optimization process is essentially to search the set of parameters that best minimizes the measure of error, as given by Eq. (11). This process is terminated at either the default number of iterations or the instance when the pre-defined value of the objective function is obtained. As the measure of error for each test is unknown prior to the PSO analysis, defining an absolute error as the termination criterion may not ensure a good fit is acquired after the entire PSO process. Therefore, in this study we used a certain number of iterations as the termination criterion of PSO.

4 Experimental program and finite element simulations

Sajid and Kiran (2018) conducted a series of tensile tests on circumferentially notched specimens made of ASTM A36, A572 Gr. 50, and A992 steels. The notched specimens for each steel included three circular notched specimens (CNs), a U-notch specimen (UN), and two V-notch specimens (VNs). In addition, conventional tensile tests on axisymmetrically unnotched specimens (SR specimens) were performed to calibrate the true stress-true strain relationship for each grade of steel. Various notched shapes were designed to achieve a wide range of stress triaxialities (within the range of 0.33–1.15) and various fracture loci. Fig. 1 provides the geometries and dimensions of the notched specimens. Detailed information about the mechanical properties of each of the three steels (such as load-displacement responses) can be found in (Sajid and Kiran, 2018). In the current study, the calibration of model parameters for ASTM steels was based entirely on the test results reported by Sajid and Kiran (2018). Three types of notched specimens (CN, UN, and VN) were used, and the identification of the fracture model parameters was conducted through CNs and UN, whereas the validation of the calibrated fracture model and the PSO algorithm was based on the test results of VNs.

Finite element simulations were carried out using the FE platform ABAQUS (Dassault Systèmes, 2016),

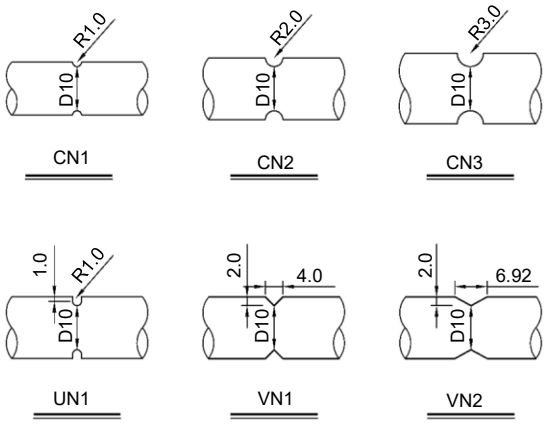

Fig. 1 Geometries and dimensions of notched specimens (CN, UN, and VN represent C-notch, U-notch, and V-notch specimens, respectively) (unit: mm)

which was used to obtain continuum stress and strain fields and to facilitate the prediction of ductile fracture using various models. Taking advantage of the symmetry, each cylindrical notched specimen was represented by a 2D axisymmetric model using the solid element CAX4, which is a fully integrated bilinear element. Only half of the specimen was modeled in this study. An illustrative FE model with the corresponding boundaries and loading conditions is shown in Fig. 2. The mesh refinement for each finite element model was selected based on mesh sensitivity studies. The size of the element in the critical regions of the specimen needed to be smaller than the characteristic length (see Section 5 for more details) to accurately capture the gradients of stress and strain fields. Consequently, elements of 0.1 mm in the critical regions and 1 mm in the remaining regions were chosen for each FE model. Material nonlinearity associated with J2 isotropic hardening was considered in the analysis.

5 Calibration of uncoupled void growth-type models

Finite element simulations provide access to the continuum stress and strain fields of each test specimen, which is required for determining the fracture initiation locus and the uncoupled fracture models. A good description of the stress and strain fields focuses on the accuracy of constitutive properties used in the continuum finite element (CFE) modeling. Characterization of material constitutive response prior to

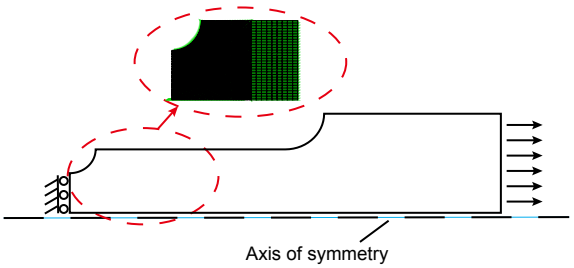

Fig. 2 Finite element model of the notched specimen

fracture initiation is crucial not only for CFE simulations, but also for calibration of the fracture criteria. As discussed previously, stress degradation due to the accumulation of damage was not considered in the constitutive law for the uncoupled fracture model. The material constitutive properties were not affected by the fracture model parameters. In this case, the calibration of the constitutive law and the fracture models can be performed separately and sequentially. Sections 5.1 and 5.2 detail the steps of calibration for the strain hardening law and void growth-type fracture models, respectively.

5.1 Strain hardening law

J2 isotropic strain hardening laws are typically used for FE modeling of structural steels. Conventional calibration of the strain hardening law (i.e., a true stress-strain curve) is commonly based on uniaxial tensile tests of SR specimens. Sajid and Kiran (2018) provided the strain hardening curves of SR specimens for all three steels, which were directly converted from engineering stress-strain relationships up to uniform deformation, and eventually extrapolated manually for the post-necking regime. To select an appropriate strain hardening law, Seupel and Kuna (2019) and Seupel et al. (2020) compared the performance of four different hardening law models (i.e., the power law, Swift law, Voce law, and Voce law with saturation to linear hardening) to represent the strain hardening behavior of steels. They found that a combination of saturating and linear terms was the best choice among the four models. Fig. 3 compares the load-elongation responses of specimen CN1 for the three steels using either the strain hardening law of Swift law or the Voce law with saturation to linear hardening, and demonstrates the superior performance of the latter. Therefore, in this study we used the Voce law with saturation to linear hardening as the strain hardening law, given as:

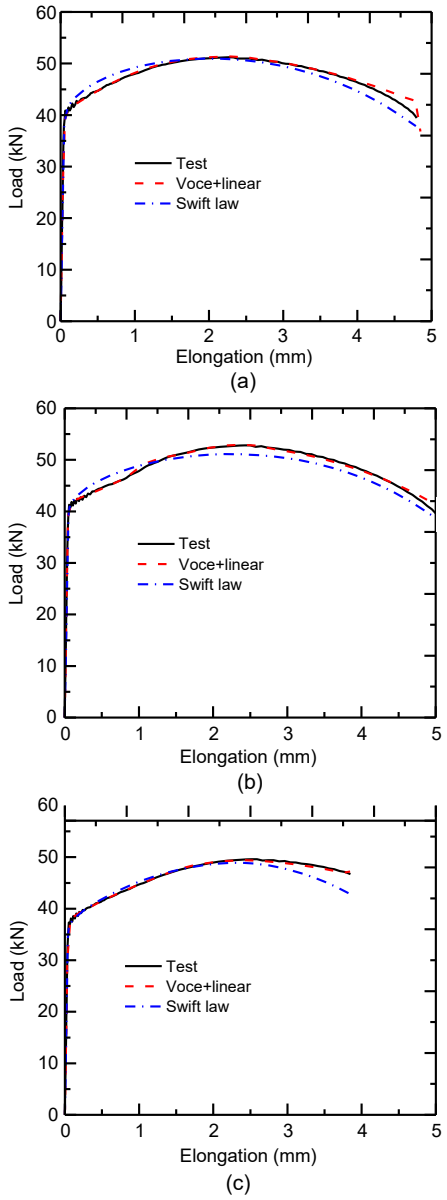

Fig. 3 Comparison of load-elongation responses of specimen CN1 for three steels using different strain hardening laws: (a) A36 steel; (b) A572 Gr. 50 steel; (c) A992 steel

$$\bar{\sigma}\left(\varepsilon_{\mathrm{eq}}\right)=\sigma_0+Q_\infty\left[1-\exp\left(-b\varepsilon_{\mathrm{eq}}\right)\right]+C\varepsilon_{\mathrm{eq}}, \quad (14)$$

where σ_0, Q_∞, b, and C are the four parameters required to be calibrated in the strain hardening law.

The experimental load-displacement responses of the four CN and UN specimens were used to construct the objective function of PSO. The parameters required for FE-PSO coupled analysis were selected following the discussion in Section 3, and are listed in Table 1. Note that the upper and lower bounds of each strain hardening parameter for a given steel, particularly the initial yield stress (σ_0), are estimated based on test results reported by Sajid and Kiran (2018). Among other parameters for the PSO algorithm, the number of particles, n_p, was first determined following the recommendation by Smith et al. (2017). As there were four parameters requiring optimization in the present problem, the value of n_p was selected to be 20. The total number of evaluations of function (i.e., the product of the number of particles and the number of iterations) has been found to be a good indicator of the rate of convergence (Vaz Jr et al., 2016). After several attempts, it was found that the value of 800 for the number of evaluations of the function was sufficient for the PSO to reach convergence. In this case, 40 iterations were carried out for each steel to ensure that the objective function was minimized before the end of the iterative process.

Fig. 4 shows the evolution of the objective function during the identification of the PSO-based strain hardening law. For a given type of steel, the objective function reduced significantly at the beginning of the PSO iterations. This was followed by a slow decrease in $\varepsilon(Z)$ for minimizing the error between the experimental and simulation results. The error became stable towards a specific value at the later stage of PSO. This implies the number of function evaluations selected in this study was large enough to find an optimal solution. The calibrated strain hardening parameters are listed in Table 1. The minimized values for $\varepsilon(Z)$ for the three steels lay within the range of 0.0179–0.0359 (an average error of 0.006–0.012 for a given CN/UN test). The simulated load-displacement response of each CN/UN specimen (Fig. 5) was modeled using the identified strain hardening law, and compared with the experimental curve. For a given specimen,

Table 1 PSO parameters and results for calibration of strain hardening laws of steels

Steel	σ_0 (MPa)			Q_∞ (MPa)			b			C (MPa)			n_p	φ_p=φ_g	w	n
	b^{lo}	b^{up}	Result	b^{lo}	b^{up}	Result	b^{lo}	b^{up}	Result	b^{lo}	b^{up}	Result				
A36	375	390	384.20	10	500	384.20	10	50	28.16	200	1000	434.08	20	1.5	From 0.55 to 0.275	40
A572 Gr. 50	380	395	391.58	10	500	391.58	10	50	17.25	200	1000	408.57				
A992	345	360	347.44	10	500	347.44	10	50	15.83	200	1000	350.13				

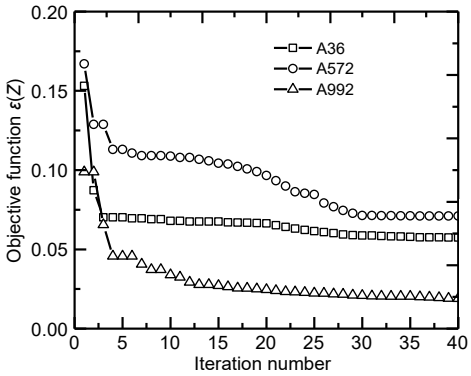

Fig. 4 Evolution of objective function in the PSO-based identification of strain hardening law

the numerical load-displacement curve showed good agreement with the test results, indicating reasonable accuracy of the strain hardening parameters calibrated using PSO.

5.2 Calibration of RT-VGM and MM-VGM

The calibration of the uncoupled fracture model parameters requires the strain and stress fields up to the initiation of ductile fracture. Fracture initiation is determined based on the experimental load-displacement response. For CNs and UN with smooth notches, after the initiation of ductile fracture, fracture propagated very rapidly in the critical regions. The point at which the load-carrying capacity suddenly dropped in the experimental load-deformation curve is well-recognized as the initiation of fracture (Kanvinde and Deierlein, 2006; Anderson, 2017). With these available stress and strain fields up to the initiation of fracture, the fracture locus of each specimen could easily be constructed. Based on this, the material toughness-related parameters in each uncoupled fracture criterion (β and VGI_{cr} for RT-VGM, and $MVGI_{cr}$ and λ for MM-VGM) were calibrated. First and foremost, the characteristic length parameter needed to be determined for each steel. As the FE-PSO coupled analysis used a constant FE mesh configuration (i.e., unchanged mesh size) that considered the characteristic length, this parameter was determined based on previous studies rather than through optimization.

Both the RT-VGM and MM-VGM criteria were required to be satisfied over a minimal material volume that was based upon the characteristic length (l^*). A widely used measure of the characteristic length is the size of the ovoid clusters (Kanvinde and Deierlein, 2006; Kiran and Khandelwal, 2014a), that is the averaged micro-cup and cone size over several void clusters. In this regard, Kanvinde and Deierlein (2006) provided estimates for the characteristic length of A572 Gr. 50 steels and found that it lay within the range 180–230 μm. Based on measurements over the fractured surface of C-notch and V-notch specimens, Kiran and Khandelwal (2014a) used a characteristic length of 200 μm for A992 steel. The characteristic length in this study was considered to be 0.2 mm for all three steels. This is reasonable because: (1) the selected value was consistent with those reported in previous studies, and (2) the accuracy of the fracture prediction was less sensitive to this parameter in situations of relatively low stress and strain gradients, such as those over the critical cross-sections in the circumferentially notched specimens.

With the strain hardening laws obtained using PSO and the estimated characteristic length (l^*), each VGM-type criterion had two remaining parameters to be determined. Similar to the calibration constitutive models, the optimization search algorithm for the fracture models required pre-defined PSO parameters. These PSO parameters included the number of particles, importance of the position of a particle and inertia weights, the number of iterations, and the initial bounds of the fracture model parameters. The algorithm-related parameters were discussed in Section 3. The model-related parameters, i.e., the two bounds, were chosen according to the values reported in previous studies. For RT-VGM, previous calibrations provided the estimated parameters VGI_{cr} and β, whose values lay within the ranges of 1.1–4.0 and 1.0–2.0, respectively, for ASTM structural steels (Kanvinde and Deierlein, 2006; Kiran and Khandelwal, 2014a). For MM-VGM, the only documented estimates of the two parameters $MVGI_{cr}$ and λ were 1.50 and 1.47, respectively, for A992 steels (Kiran and Khandelwal, 2013). Based on these results, broader ranges were used in this study as the bounds of the RT-VGM and MM-VGM parameters that initiated the PSO process (Table 2). The optimization results are listed in Table 2. Note that the estimated β values for A572 Gr. 50 and A992 steels were comparable to those reported by Kanvinde and Deierlein (2006) and Kiran and Khandelwal (2014a), who suggested values of 1.18 for A572 Gr. 50 steel and 1.15 for A992 steel. The parameter λ was found to have the value of 1.6 for A36 steel, and 1.4 for both A572 Gr. 50 and A992

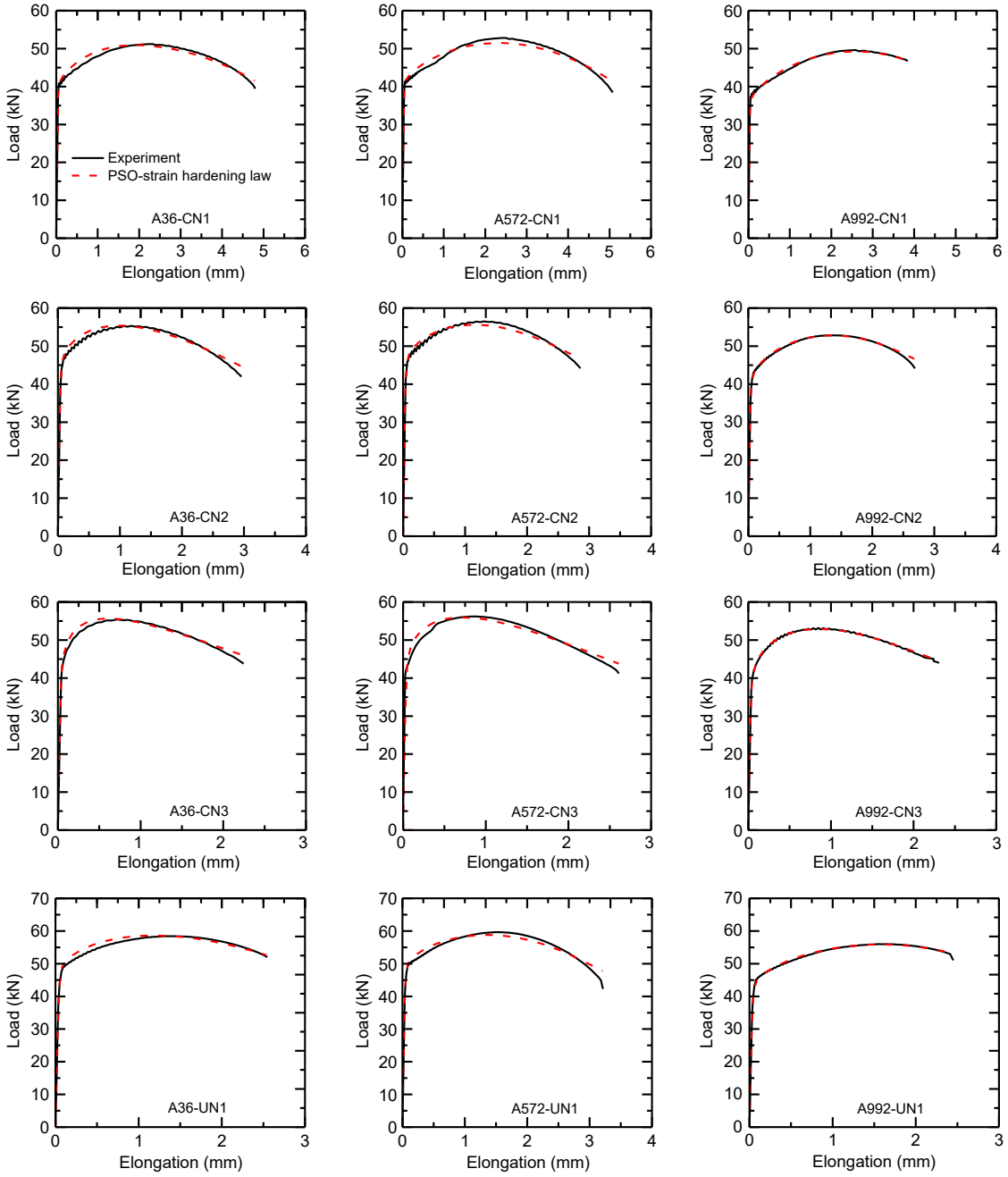

Fig. 5 Experimental and predicted load-displacement curves of A36, A572 Gr. 50 (A572), and A992 steels

Table 2 PSO parameters used for calibration of RT-type fracture models

Steel	Model	β or λ			VGI_{cr} or $MVGI_{cr}$			n_p	$\varphi_p=\varphi_g$	w	n
		$\boldsymbol{b}^{lo}$	$\boldsymbol{b}^{up}$	Result	$\boldsymbol{b}^{lo}$	$\boldsymbol{b}^{up}$	Result				
A36	RT-VGM	0.5	2.0	1.52	1.0	6.0	2.81	10	1.5	From 0.55 to 0.275	20
	MM-VGM	0.5	3.0	1.03	0.1	6.0	0.57				
A572 Gr. 50	RT-VGM	0.5	2.0	1.61	1.0	6.0	3.23	10	1.5	From 0.55 to 0.275	20
	MM-VGM	0.5	3.0	1.13	0.1	6.0	0.69				
A992	RT-VGM	0.5	2.0	1.06	1.0	6.0	1.53	10	1.5	From 0.55 to 0.275	20
	MM-VGM	0.5	3.0	1.39	0.1	6.0	0.72				

steel. As mentioned earlier, the reported value of parameter λ for A992 steel was constant at 1.47 (Kiran and Khandelwal, 2013), which was ratified by the results obtained using the PSO search algorithm in this study.

6 Calibration of the GTN model

The calibration of the GTN model was implemented using automated PSO. PSO-based optimized calibration of the GTN model required the input parameters, including the strain hardening properties and the upper and lower bounds of each GTN model parameter. A detailed strategy to determine the parameters used to initialize the PSO is provided below.

According to Cuesta et al. (2010) and Kiran and Khandelwal (2014c), the plastic region of the load-displacement curve for a given steel tensile round specimen can generally be divided into four stages (Fig. 6):

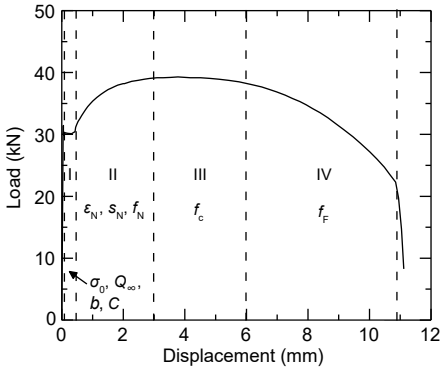

Fig. 6 Stages in load-displacement curve of a typical steel tensile round specimen

(1) Stage I: This stage refers to the initial stage of plasticity, and is controlled mainly by the constitutive relation. At this stage, damage is not accumulated before the initiation of the void. The initial porosity f_0 has an insignificant influence on the global response of the specimen.

(2) Stage II: Void nucleation begins at the nucleation strain (ε_N). The rate of the accumulation of damage is governed mainly by the parameters ε_N, s_N, and f_N.

(3) Stage III: Growth of the void accelerates once the void volume fraction reaches the critical void volume parameter (f_c). At this stage, the rapid void growth is associated with a sudden degradation of the strength of the material. The quick loss of material strength is considered terminated when the modified void volume fraction reaches the parameter f_F.

(4) Stage IV: Because at certain points across the critical cross-section of the round specimen, the material has completely lost strength, a part of the specimen has already separated. A sudden drop in the load-carrying capacity occurs when a sufficient number of points on the material lose strength, and softening due to void coalescence (material failure) compensates for the hardening at other material points.

First, based on a thorough literature review, the initial porosity f_0 was determined. According to previous studies (Table 3), it was found that very small values were used for the initial porosity f_0. As initial porosity has a negligible effect on the first stage in the load-displacement curve, we assumed that there was no pre-existing void before material was loaded, and the growth of the porosity was completely due to the nucleation of new voids. In this study, the initial porosity f_0 was considered as 0 for all three steels (Kiran and Khandelwal, 2013).

Second, the Voce law with saturation to linear hardening was adopted as the yield stress of the fully dense matrix material, i.e., the strain hardening law. The strain hardening law is typically determined from the pre-necking load-displacement response of SR specimens, and assumes that the changes in porosity and porosity-induced damage are both negligible up to uniform deformation in the specimen (Cuesta et al., 2010; Abbasi et al., 2012a, 2012b; Kossakowski, 2012; Kiran and Khandelwal, 2013). As the initial porosity f_0 was considered to be zero in this study, the strain hardening law used in the GTN model was obtained directly from the measured pre-necking load-displacement curve of SR specimens by Sajid and Kiran (2018). The strain hardening parameters were determined by fitting the reported true stress-plastic strain curve up to necking. The calculated strain hardening law parameters for each steel are listed in Table 4.

Third, the bounds of the eight GTN parameters to initialize PSO were selected based on previous studies (Table 3). Note that the parameters for the yield condition (q_1, q_2, and q_3) were estimated based on the recommendation by ABAQUS (Dassault Systèmes, 2016), and had the values of $0.9 \leqslant q_1, q_2 \leqslant 1.6$. Moreover, these GTN parameters were evaluated through three trials of PSO run, which means that the PSO was run using various parameter bounds to search

Table 3 GTN model parameters in the literature

Reference	Material	q_1	q_2	q_3	f_0	f_c	f_F	f_N	ε_N	s_N
Abbasi et al. (2012b)	IF-steel	1.5	1	2.25	0.005	0.02	0.05	0.01	0.08	0.06
Abbasi et al. (2012a)	Monolithic Blank	1.5	1	2.25	0.0002	0.0134	0.0216	0.0106	0.1	0.1
Kossakowski (2012)	S235JR steel	1.5	1	2.25	0.0017	0.06	0.667	0.04	0.3	0.05
Abbassi et al. (2013)	Mild steel	1.5	1	2.25	0.003	0.08	0.12	0.04	0.3	0.22
Yan et al. (2013)	Silicon steel	1.55	0.9	2.40	0.0025	0.101	0.155	0.04	0.24	0.01
Kiran and Khandelwal (2014c)	A992 steel	1.5	1	2.25	0	0.03	0.5	0.02	0.45	0.05
Mansouri et al. (2014)	Mild steel	1.5	1	2.15	0.001	0.0601	0.2170	0.039	0.21	0.1
	Al5182	1.5	1	2.15	0.001	0.00213	0.0864	0.035	0.270	0.1
	Al5754	1.5	1	2.15	0.001	0.00284	0.1231	0.034	0.320	0.1
	Al6016	1.5	1	2.15	0.001	0.01520	0.0705	0.036	0.276	0.1
	XES steel	1.5	1	2.15	0.001	0.04	0.2010	0.040	0.500	0.1
	ULC/Ti	1.5	1	2.15	0.001	0.04	0.2010	0.040	0.500	0.1
Cha and Kim (2014)	DP780	1.5	1	2.25	0.003	0.013	0.207	0.018	0.102	0.206
Teng et al. (2014)	AA5A02	1.5	1	2.25	0.001	0.02	0.0363	0.0242	0.1	0.1
Kami et al. (2015)	AA6016-T4	1.5	1	2.25	0.00035	0.05	0.15	0.05	0.3	0.1
Yu et al. (2014)	AA6061-T6	1.5	1	2.25	0.000125	0.013	0.04	0.0008	0.3	0.1
Li JC et al. (2015)	DC06 steel	1.5	1	2.25	0.001	0.04	0.06	0.004	0.3	0.1
Gatea et al. (2015)	Pure Ti	1.5	1	2.25	0.00138	0.2593	0.3025	0.017	0.3	0.1
Li H et al. (2015)	AA2024-T351	1.25	1	1.56	0.1	0.25	0.5	–	–	–
Sun et al. (2015)	AA2219-T6	1.5	1.25	2.25	0.00328	0.011	0.015	0.01	0.12	0.3
Zhong et al. (2016)	3Cr1MoV	0.608	0.562	0.369	0	0.24	0.261	0.179	0.124	0.083
Zhao et al. (2016)	DP600	1.5	1	2.25	0.0008	0.028	0.09	0.02	0.2	0.1
Zhang and Cong (2016)	SUS304 sheet	1.5	1	2.25	0.002	0.11	0.156	0.032	0.54	0.09
Amaral et al. (2016)	AA5182-O	1.5	1	2.25	0.01	0.021	0.04	0.001	0.3	0.1
Wang and Li (2017)	BR1500HS	1.5	1	2.25	0.005	0.2324	0.3071	0.04	0.3	0.1
Yuenyong et al. (2018)	SS304	1.5	1	2.25	0.00183	0.0135	0.2628	0.0056	0.3	0.1
Kumar et al. (2017)	SS304LN	1.5	1	2.25	0.00001	0.11	0.25	0.006	0.3	0.1
Teng et al. (2017)	AA5A06	1.5	1	2.25	0.0012	0.034	0.042	0.032	0.25	0.08
Nguyen et al. (2018)	AA6061-T6 (2-mm thin sheet)	1.321	0.948	2.582	0.0016	0.087	0.140	0.052	0.115	0.054
	AA6061-T6 (25-mm thick sheet)	1.255	1.053	3.893	0.0018	0.022	0.111	0.058	0.64	0.052
Ying et al. (2018)	22MnB5	1.5	1	2.25	0.002	0.05	0.13	0.0155	0.3	0.1
Ali and Huang (2019)	AZ61 Mg	1.5	1	2.25	–	0.18	0.2	0.078	0.2	0.0064
Sun et al. (2020)	Silicon steel	1.5	1.0	2.25	0.002	0.234	0.351	0.217	0.344	0.1
Zhang et al. (2018)	Nuclear piping steel	1.5	1.07	2.25	0.0002	0.05	–	0	–	–
Zhang et al. (2021)	STPT410 steel	1.225	0.91	1.50	0.0003	0.08	0.1	0.047	0	0.049
Kulawinski et al. (2020)	27NiCrMoV15-6 steel	1.5	1.0	2.25	0.001	0.057	0.114	0.006	0.36	0.12
Soyarslan et al. (2016)	P91 steel	1.5	1.0	2.25	0.00044	0.1	0.25	0.02	0.3	0.1
Brinnel et al. (2015)	P500Q steel	1.5	1.0	2.25	0.001	0.15	0.52	0	0	0
Linse et al. (2014)	A533B Cl.1 steel	1.5	1.0	2.25	0.00023	0.0375	0.2	0.023	0.16	0.1
Haušild et al. (2002)	A508 Cl.3 steel	1.5	1.0	2.25	0.0005	0.01	0.755	0.006	0.3	0.1
Rossoll et al. (2002)	A508 Cl.3 steel	1.5	1.0	2.25	0.005	0.06	0.21	0.25	0.3	0.1
Eberle et al. (2000)	StE 460 steel	1.5	1.0	2.25	0.0025	0.021	0.19	0.01	0.3	0.1
Steglich and Brocks (1998)	Nodular cast iron	1.5	1.0	2.25	0.114	0.175	0.235	–	–	–
Bernauer and Brocks (2002)	DIN22 NiMoCr 37 steel	1.5	1.0	2.25	0.002	0.0048–0.063	0.20	–	–	–

the best solution, as suggested by Smith et al. (2017). The three trials also served to determine the PSO parameters (n_p and n). Based upon a literature review and multiple attempts of PSO analysis, all the parameters required for PSO calibration were chosen (Table 4).

Similar to the uncoupled models, notches CN1, CN2, CN3, and UN1 were used for calibrating the GTN model parameters. The calibrated GTN parameters along with the minimized objective functions for each of the three steels are listed in Table 5. Fig. 7 compares the experimental and numerical load-displacement curves for each specimen and steel type. Note that only the experimental response up to fracture initiation is shown in Fig. 7. The predicted response was calculated using the optimized GTN parameters given in Table 5.

The comparison shown in Fig. 7 demonstrates that PSO provided a favorable calibration for the yield function related parameters q_i (i=1, 2, 3) and the void nucleation related parameters ε_N, s_N, and f_N. This was based on the observation that the responses of Stages I and II in the load-displacement curve were in good agreement with the test results for each specimen (generally before the peak load). Although the numerical prediction matched the experimental results with respect to Stages III and IV (post-peak regime) in the load-displacement curve, which were controlled by the two parameters f_c and f_F, the numerical results were spuriously mesh-dependent. This is because the GTN model adopted in this study was based on a common local approach (Kiran and Khandelwal, 2013; Vaz Jr et al., 2016; Zhu and Engelhardt, 2018a). The softening stage of the load-displacement response, as calculated by the local version of GTN, is well recognized to diverge upon mesh refinement (Kiran and Khandelwal, 2013; Vaz Jr et al., 2016; Zhu and Engelhardt, 2018a). However, the damage was at a relatively low level during most of the loading process, and the degradation occurred only at the end of the deformation history in each specimen. The calibrated GTN parameters may be acceptable as a phenomenological estimate of the material degradation property. A better approach to address the mesh dependency issue is to use a nonlocal-type or gradient-enhanced GTN model (Li H et al., 2015; Zhu and Engelhardt, 2018a; Seupel et al., 2020).

7 Validation and discussion

The calibrated ductile fracture models were validated using the test results of the V-notch specimens. The evaluation focused not only on the initiation of ductile fracture, but also on the full range of the load-displacement response. The comparison of the void growth damage index (VGI or MVGI) with the critical value of the counterpart along the critical cross-section determined the predicted initiation of ductile fracture using the uncoupled models. The location at which the element first reached the failure porosity f_F was considered as the fracture initiation using the GTN model.

Fig. 8 compares the experimental and numerical load-displacement curves of the two V-notch specimens, as computed by the PSO-calibrated strain hardening law and the GTN constitutive relation. The strain hardening law provided a good prediction of the load-displacement response of each V-notch, except for the later stage of the loading history. The results show that the experimental load-elongation curves dropped off more rapidly. Unlike notches with smooth roots

Table 4 PSO parameters used for calibration of GTN model

Steel	σ_0 (MPa)	Q_∞ (MPa)	b	C (MPa)	q_1, q_2		s_N, ε_N		f_N		f_c		f_F		n_p	$\varphi_p=\varphi_g$	w	n
					$\boldsymbol{b}^{lo}$	$\boldsymbol{b}^{up}$	$\boldsymbol{b}^{lo}$	$\boldsymbol{b}^{up}$	$\boldsymbol{b}^{lo}$	$\boldsymbol{b}^{up}$	$\boldsymbol{b}^{lo}$	$\boldsymbol{b}^{up}$	$\boldsymbol{b}^{lo}$	$\boldsymbol{b}^{up}$				
A36	379.7	239.0	12.33	0	0.9	1.6	0.1	0.5	0	0.15	0	0.2	0.01	0.9	30	1.5	From 0.55 to 0.275	30
A572 Gr. 50	377.4	272.3	11.41	0	0.9	1.6	0.1	0.5	0	0.15	0	0.2	0.01	0.9				
A992	342.4	244.3	14.72	12.7	0.9	1.6	0.1	0.5	0	0.15	0	0.3	0.01	0.85				

Table 5 Calibrated parameters of GTN model for A36, A572 Gr. 50, and A992 steels

Steel	q_1	q_2	q_3	f_0	s_N	f_N	ε_N	f_c	f_F	$\varepsilon(Z)$
A36	1.14	0.92	1.300	0	0.36	0.007	0.098	0.20	0.26	0.0236
A572 Gr. 50	0.76	1.14	0.578	0	0.56	0.061	0.41	0.27	0.60	0.0359
A992	1.31	1.00	1.710	0	0.23	0.012	0.40	0.18	0.48	0.0179

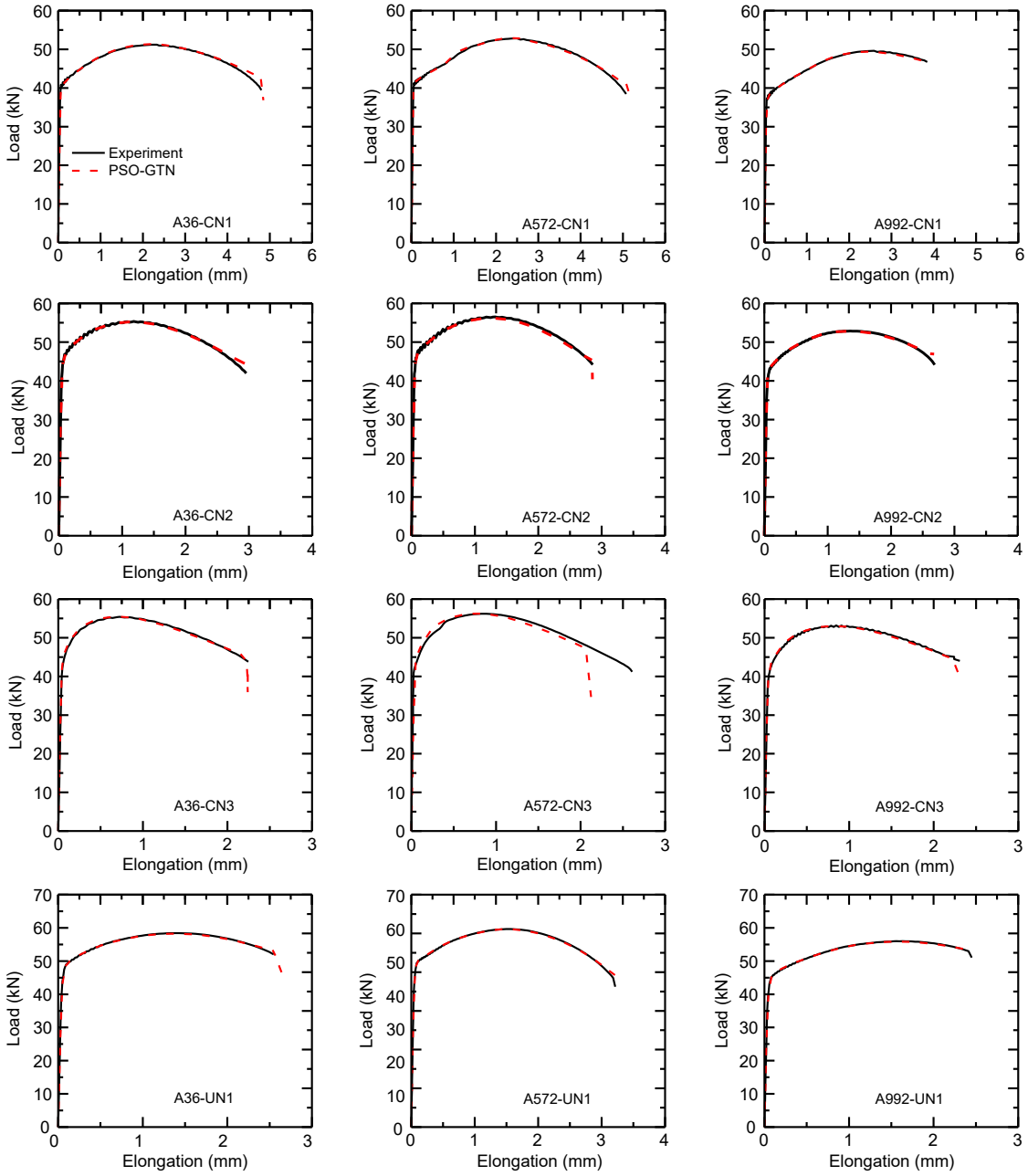

Fig. 7 Comparison of experimental load-displacement curves and numerical results by the GTN model

(e.g., C- and U-notches), V-notches have a man-made stress concentration at the sharp tip. As a result, accumulation of damage due to void nucleation and growth mechanisms in V-notches may be more significant than in C- and U-notches (Kiran and Khandelwal, 2013). However, the present uncoupled models were incapable of adequately representing the damage-induced softening in VNs. A possible improvement to mitigate the issue is to introduce phenomenological damage evolution laws to the current fracture criteria (Kiran and Khandelwal, 2014b; Jia et al., 2016; Yan et al., 2018) to describe the gradual stress degradation of the material following the initiation of ductile fracture until the complete loss of strength. Regardless of this drawback, the predicted displacements at fracture initiation by the two uncoupled models matched reasonably well for all six V-notches, and the relative errors were well within 13% (Fig. 9).

Fig. 10 shows the plastic strain contours of the VN1 and VN2 specimens near fracture initiation

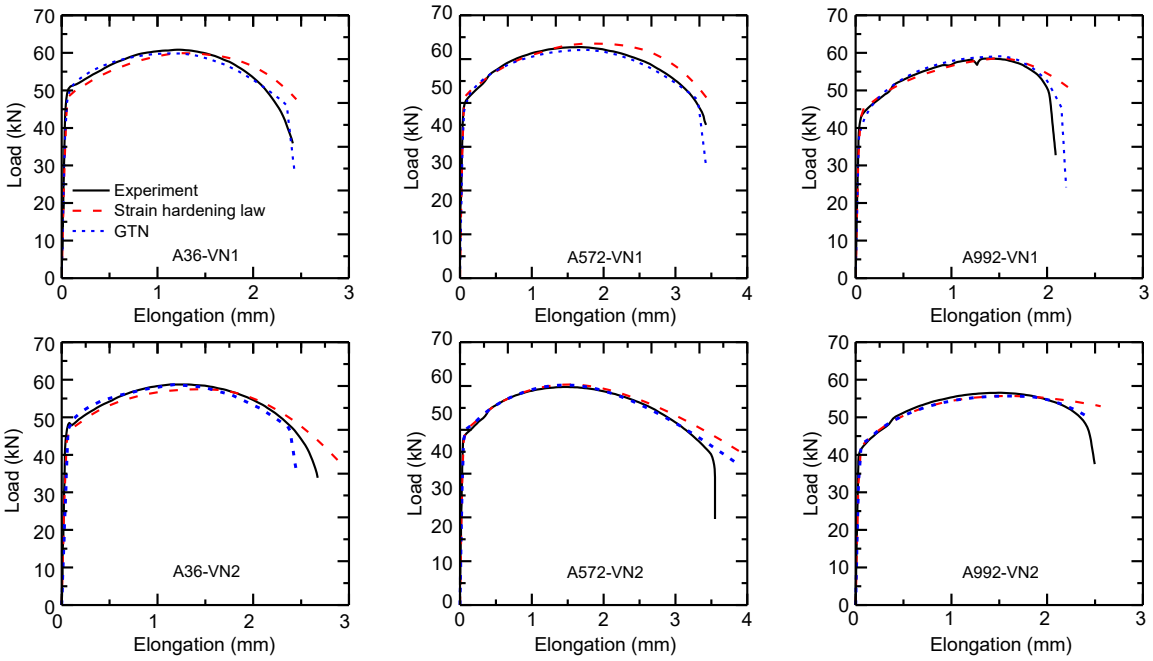

Fig. 8 Experimental and numerical load-displacement curves for the V-notch specimens

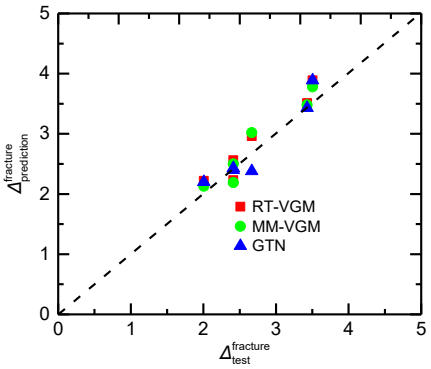

Fig. 9 Comparison of experimental and numerical prediction of fracture initiation in V-notches using RT-VGM, MM-VGM, and GTN model ($\Delta^{\text{fracture}}_{\text{test}}$ and $\Delta^{\text{fracture}}_{\text{prediction}}$ represent the experimental and predicted displacement to fracture initiation, respectively)

for the three steels. Strain concentration is apparent at each V-notch with a high strain gradient. Note that the distribution of stress triaxiality is smooth along the critical radius, and peaks near the region of strain concentration. The fracture locations predicted by both RT-VGM and MM-VGM are coincident with the site of strain concentration, i.e., near the V-notches. The predicted sites of fracture initiation are consistent with experimental observation using fracture tests similar to those of Kiran and Khandelwal (2013). Fig. 11 compares the fracture loci constructed by the two uncoupled fracture models with the test results. The parameter T_{avg} in Fig. 11 represents the average stress triaxiality during the plastic strain history (Kiran and Khandelwal, 2013; Wen and Mahmoud, 2016; Zhu and Engelhardt, 2018b). The two uncoupled models showed acceptable accuracy in predicting the fracture strain of the V-notch specimens. In general, MM-VGM performed better than RT-VGM in predicting fracture at a triaxiality lower than 1.1, while RT-VGM provided more accurate predictions for fractures at higher triaxialities.

In contrast to the two uncoupled models, the GTN model considers the continuous degradation of material strength attributed to the nucleation and growth of voids. This is an advantage over the uncoupled models in representing the damage-induced drop of load carrying capacity. As a result, based upon the GTN model, the predicted load-displacement response at the later stage matched the test results better than the PSO-calibrated strain hardening law (Fig. 8). Regarding the softening part of the load-displacement curve, deviation of the numerical results predicted by the strain hardening law from the experimental results and the results predicted by GTN emphasizes the great importance of the coupled model in describing the softening behavior of the CNT specimen. From the perspective of numerical practice, the GTN model used in this study had a spurious mesh dependence issue. The predicted load-displacement response at the

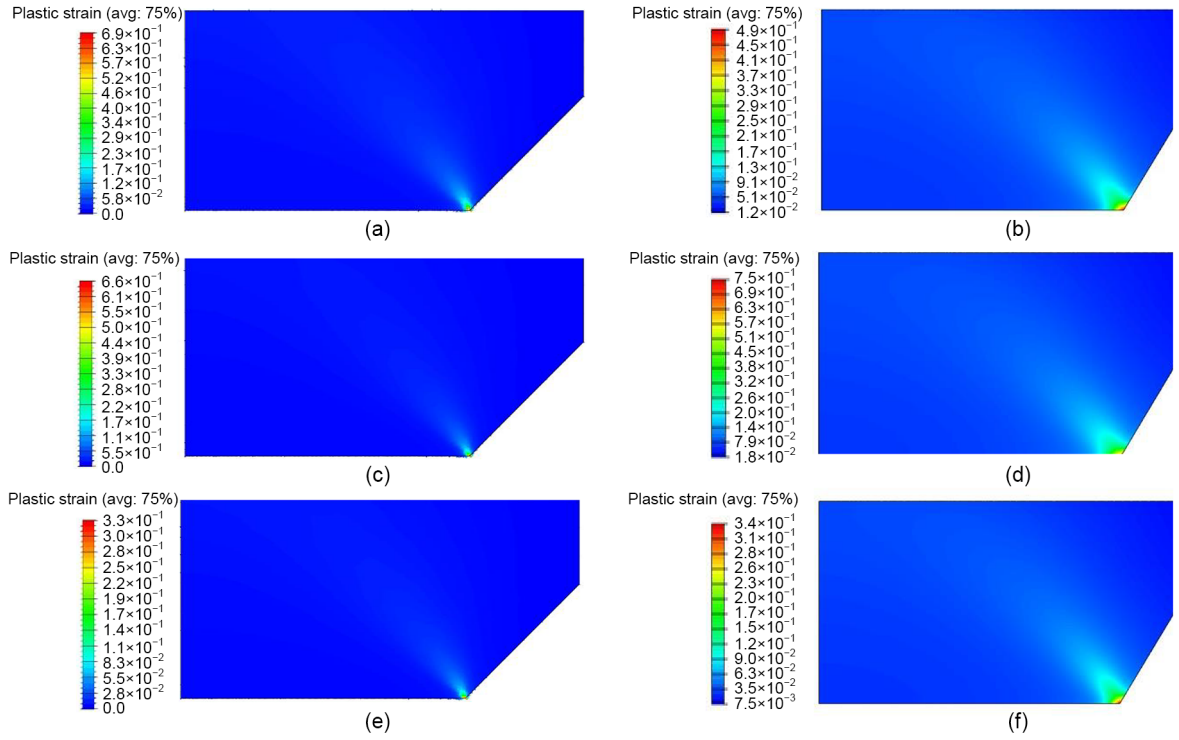

Fig. 10 Plastic strain contours for the VN1 and VN2 specimens near fracture initiation: (a) A36-VN1; (b) A36-VN2; (c) A572-VN1; (d) A572-VN2; (e) A992-VN1; (f) A992-VN2

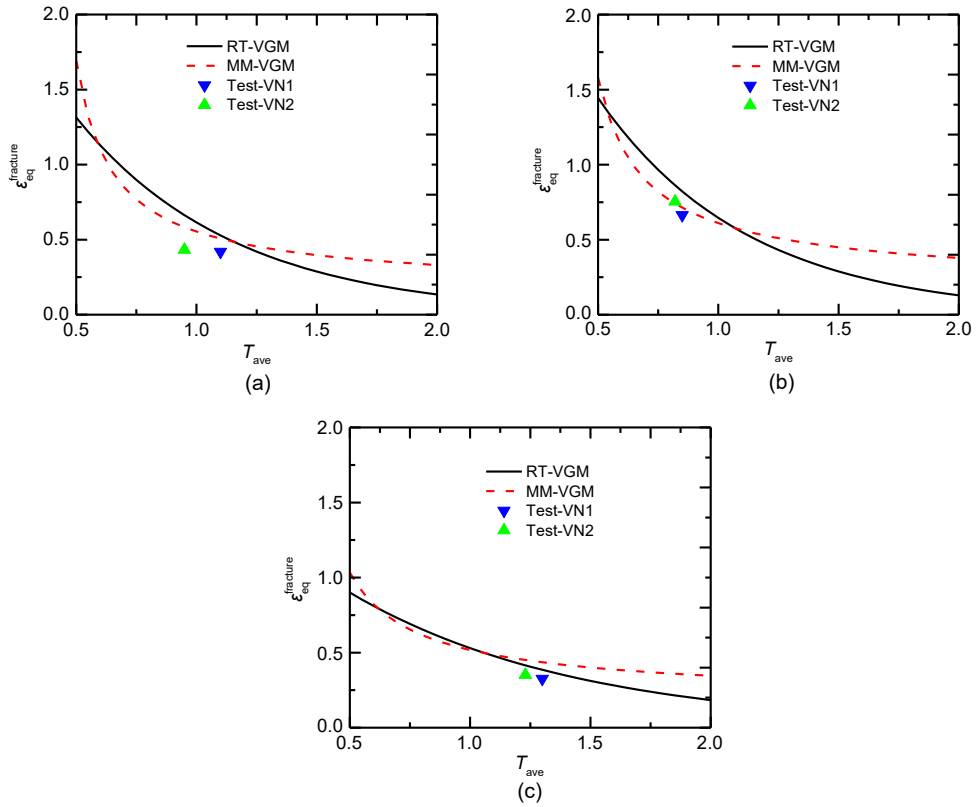

Fig. 11 Comparison of fracture loci constructed by RT-VGM and MM-VGM with the test results: (a) A36 steel; (b) A572 Gr. 50 steel; (c) A992 steel ($\varepsilon_{eq}^{fracture}$ represents the equivalent plastic strain to fracture initiation)

softening stage was intrinsically mesh sensitive, and decreasing the mesh size did not result in numerical convergence. This caused the predicted fracture initiation in V-notches using the GTN model to become mesh dependent, indicating that the predicted displacement to fracture initiation diverged upon mesh refinement. Nevertheless, the PSO-calibrated GTN model showed good performance in representing the damage-coupled constitutive relation for all three steels before the initiation of ductile fracture. Future work to compensate for the current limitations and to provide mesh-independent prediction of ductile fracture initiation could incorporate a regularization treatment to the local version of GTN, i.e., introducing an internal length parameter.

The validation study also illustrated the robustness of the PSO approach in identifying the ductile fracture model parameters. By using several notched specimens, the automated calibration procedure gave rise to estimated parameters that were more objective, and resulted in acceptable predictive performance of the present fracture models. Irrespective of the number of parameters to be determined, the PSO algorithm was applicable not only for the uncoupled models associated with the strain hardening law, but also for the coupled GTN model. Although the calibration of the fracture model required thousands of FE simulations and dozens of hours (e.g., 4 specimens×20 particles×40 iterations=3200 simulations and 25 h to execute on a 3.60-GHz ordinary desktop), PSO still had an advantage in computational cost over other advanced computing algorithms, e.g., NN, RS, and GD. To acquire an accurate result from the calibration problem, NN requires a greater number of samples for training (e.g., at least 4 specimens×3^8≈26000 FE simulations for the 8-parameter GTN calibration) than the PSO algorithm (i.e., 4 specimens×30 particles×30 iterations=3600 simulations for the same problem). The RS method is also likely computationally expensive, requiring three times more evaluations of the objective function than the PSO. The GD-like gradient methods are extremely sensitive to the discontinuous objective functions (the complex interface between FE package and MATLAB script to calculate the objective function makes the error function not smooth), and require detailed handling of error. Besides, the high-dimensional search-space and the complex exchanges among multiple software packages (e.g., ABAQUS, MATLAB, Python) make gradient computation and other optimization approaches (e.g., Levenberg-Marquardt algorithm) less efficient and more challenging. The lower computational demand of FE simulations by PSO compared to other classical search approaches, and its favorable predictive accuracy (as illustrated in Figs. 10 and 11) emphasize that PSO has great potential for the identification of other fracture models, e.g., the shear-modified GTN model (Bernauer and Brocks, 2002; Ying et al., 2018) and the continuum damage mechanics (CDM) theory-based Lemaitre damage model (Lemaitre, 1985; Rousselier, 1987).

8 Conclusions

This paper provides an automated PSO method for calibrating the constitutive and ductile fracture model parameters of ASTM A36, A572 Gr. 50, and A992 structural steels. Three popular ductile fracture models were presented: the RT-VGM, the MM-VGM, and the GTN model. The performance of the automated parameter identification approach and the calibrated ductile fracture models was evaluated using experiments on circumferential V-notch specimens. The conclusions of the present study are as follows:

1. PSO offers a more robust identification process for the strain hardening law parameters than the conventional trial-and-error operation. PSO showed good performance in terms of both the accuracy and efficacy of the calibration process without any manual intervention. It also allowed the overall behavior of a material in the full stress-strain paths to be captured, particularly at large plastic deformations and under non-uniform stress states. However, one significant drawback of the automated calibration is that the strain hardening law (represented by a closed-form function), as determined by the PSO search algorithm, poorly described the yield plateau of the actual engineering stress-strain response of the three steels. This may be improved by introducing a piecewise polynomial strain hardening law to represent various stages of the plastic response of the steel material.

2. Each uncoupled ductile fracture model parameter was identified using a two-step PSO calibration scheme. The strain hardening law and the fracture model were determined successively based on a series

of round notched specimens. In the two uncoupled fracture models, the characteristic length was estimated as constant and the calibration process involved only two fracture toughness properties. To search the optimal fracture model parameters, the difference between the experimental and numerical displacements to fracture initiation was selected as the measure of the error (objective function) and was minimized using the PSO algorithm. The whole process of the two-step PSO analysis is fully automatic, so that only the PSO parameters are required to initiate the search algorithm.

3. The GTN model was calibrated for all the three steels using the PSO method. According to previous studies, the initial porosity f_0 was assumed to be negligible (i.e., f_0=0) for the three steels. The upper and lower bounds of the other GTN parameters required for PSO were determined based on the values used in the literature and associated with various trials of PSO calibration. The PSO analysis gave an effective calibration process. The objective function (the measure of the error) was minimized after a small number of iterations for a given steel. However, more particles may be required in the PSO process than in the calibration of the strain hardening law parameters, as the GTN model has eight parameters involved in the identification procedure. The numerical results obtained using the GTN model were in good agreement with the experimental results with regards to the load-displacement response and the initiation of the ductile fracture for each V-notch specimen.

4. Although initiation of the ductile fracture was predicted accurately, the calibrated models in this study showed obvious deficiencies. The uncoupled models were incapable of representing the damage accumulation after fracture initiation in the notched specimens, thus often overestimating the load-carrying capacity at the later stage of the loading history. The original GTN model exhibited a spurious mesh dependency issue in that the computed softening part in the load-displacement curve diverged upon mesh refinement. Solutions to these issues that can improve the predictive accuracy of the fracture models include (1) using damage evolution law in the uncoupled fracture models and (2) introducing nonlocal regularization treatment to the current GTN model. Beside the damage law-incorporated uncoupled models and the nonlocal regularized GTN models, the powerful PSO search algorithm has significant potential to calibrate other popular ductile fracture models that are applicable to predict ductile fracture over a wider range of triaxiality, e.g., models with triaxiality and Lode dependence.

Acknowledgments

This work is supported by the National Natural Science Foundation of China (No. 51908416), the Shanghai Pujiang Program (No. 19PJ1409500), and the Fundamental Research Funds for the Central Universities, China. The authors would like to particularly thank Ravi KIRAN (North Dakota State University, USA) for sharing test data.

Author contributions

Ya-zhi ZHU and Shi-ping HUANG designed the research. Hao HONG processed the corresponding data. Ya-zhi ZHU wrote the first draft of the manuscript. Shi-ping HUANG helped to organize the manuscript. Hao HONG revised and edited the final version.

Conflict of interest

Ya-zhi ZHU, Shi-ping HUANG, and Hao HONG declare that they have no conflict of interest.

References

Abbasi M, Shafaat MA, Ketabchi M, et al., 2012a. Application of the GTN model to predict the forming limit diagram of IF-steel. *Journal of Mechanical Science and Technology*, 26(2):345-352. https://doi.org/10.1007/s12206-011-1038-z

Abbasi M, Bagheri B, Ketabchi M, et al., 2012b. Application of response surface methodology to drive GTN model parameters and determine the FLD of tailor welded blank. *Computational Materials Science*, 53(1):368-376. https://doi.org/10.1016/j.commatsci.2011.08.020

Abbassi F, Mistou S, Zghal A, 2013. Failure analysis based on microvoid growth for sheet metal during uniaxial and biaxial tensile tests. *Materials & Design*, 49:638-646. https://doi.org/10.1016/j.matdes.2013.02.020

Abendroth M, Kuna M, 2006. Identification of ductile damage and fracture parameters from the small punch test using neural networks. *Engineering Fracture Mechanics*, 73(6): 710-725. https://doi.org/10.1016/j.engfracmech.2005.10.007

Ali AN, Huang SJ, 2019. Ductile fracture behavior of ECAP deformed AZ61 magnesium alloy based on response surface methodology and finite element simulation. *Materials Science and Engineering: A*, 746:197-210. https://doi.org/10.1016/j.msea.2019.01.036

Amaral R, Teixeira P, Azinpour E, et al., 2016. Evaluation of ductile failure models in sheet metal forming. *MATEC Web of Conferences*, 80:03004. https://doi.org/10.1051/matecconf/20168003004

Anderson TL, 2017. Fracture Mechanics: Fundamentals and Applications, 3rd Edition. CRC Press, Boca Raton, USA.

https://doi.org/10.1201/9781315370293

Benzerga AA, Leblond JB, 2010. Ductile fracture by void growth to coalescence. *Advances in Applied Mechanics*, 44:169-305. https://doi.org/10.1016/S0065-2156(10)44003-X

Bernauer G, Brocks W, 2002. Micro-mechanical modelling of ductile damage and tearing–results of a European numerical round robin. *Fatigue & Fracture of Engineering Materials & Structures*, 25(4):363-384. https://doi.org/10.1046/j.1460-2695.2002.00468.x

Bridgman PW, 1964. Studies in Large Plastic Flow and Fracture. Harvard University Press, London, UK. https://doi.org/10.4159/harvard.9780674731349

Brinnel V, Langenberg J, Kordtomeikel F, et al., 2015. Numerical derivation of strain-based criteria for ductile failure: discussions on sensitivity and validity. *Engineering Fracture Mechanics*, 148:421-440.

Cha WG, Kim N, 2014. Quantification of micro-cracks on the bending surface of roll formed products using the GTN model. *Metals and Materials International*, 20(5):841-850. https://doi.org/10.1007/s12540-014-5008-8

Chu CC, Needleman A, 1980. Void nucleation effects in biaxially stretched sheets. *Journal of Engineering Materials and Technology*, 102(3):249-256. https://doi.org/10.1115/1.3224807

Cuesta II, Alegre JM, Lacalle R, 2010. Determination of the Gurson–Tvergaard damage model parameters for simulating small punch tests. *Fatigue & Fracture of Engineering Materials & Structures*, 33(11):703-713. https://doi.org/10.1111/j.1460-2695.2010.01481.x

Dassault Systèmes , 2016. ABAQUS Analysis User's Manual. Dassault Systèmes Simulia, Providence, USA.

Defaisse C, Mazière M, Marcin L, et al., 2018. Ductile fracture of an ultra-high strength steel under low to moderate stress triaxiality. *Engineering Fracture Mechanics*, 194: 301-318. https://doi.org/10.1016/j.engfracmech.2017.12.035

Eberhart R, Kennedy J, 1995. A new optimizer using particle swarm theory. Proceedings of the 6th International Symposium on Micro Machine and Human Science, p.39-43. https://doi.org/10.1109/MHS.1995.494215

Eberle A, Klingbeil D, Schicker J, 2000. The calculation of dynamic J_R-curves from the finite element analysis of a Charpy test using a rate-dependent damage model. *Nuclear Engineering and Design*, 198(1-2):75-87. https://doi.org/10.1016/S0029-5493(99)00281-2

Gatea S, Lu B, Ou HG, et al., 2015. Numerical simulation and experimental investigation of ductile fracture in SPIF using modified GTN model. *MATEC Web of Conferences*, 21:04013. https://doi.org/10.1051/matecconf/20152104013

Gurson AL, 1977. Continuum theory of ductile rupture by void nucleation and growth: part I—yield criteria and flow rules for porous ductile media. *Journal of Engineering Materials and Technology*, 99(1):2-15. https://doi.org/10.1115/1.3443401

Hancock JW, Brown DK, 1983. On the role of strain and stress state in ductile failure. *Journal of the Mechanics and Physics of Solids*, 31(1):1-24. https://doi.org/10.1016/0022-5096(83)90017-0

Haušild P, Nedbal I, Berdin C, et al., 2002. The influence of ductile tearing on fracture energy in the ductile-to-brittle transition temperature range. *Materials Science and Engineering: A*, 335(1-2):164-174. https://doi.org/10.1016/S0921-5093(01)01913-X

Jia LJ, Ikai T, Shinohara K, et al., 2016. Ductile crack initiation and propagation of structural steels under cyclic combined shear and normal stress loading. *Construction and Building Materials*, 112:69-83. https://doi.org/10.1016/j.conbuildmat.2016.02.171

Kami A, Dariani BM, Vanini AS, et al., 2015. Numerical determination of the forming limit curves of anisotropic sheet metals using GTN damage model. *Journal of Materials Processing Technology*, 216:472-483. https://doi.org/10.1016/j.jmatprotec.2014.10.017

Kanvinde AM, Deierlein GG, 2006. The void growth model and the stress modified critical strain model to predict ductile fracture in structural steels. *Journal of Structural Engineering*, 132(12):1907-1918. https://doi.org/10.1061/(ASCE)0733-9445(2006)132:12

Khandelwal K, El-Tawil S, 2007. Collapse behavior of steel special moment resisting frame connections. *Journal of Structural Engineering*, 133(5):646-655. https://doi.org/10.1061/(ASCE)0733-9445(2007)133:5(646)

Kiran R, Khandelwal K, 2013. A micromechanical model for ductile fracture prediction in ASTM A992 steels. *Engineering Fracture Mechanics*, 102:101-117. https://doi.org/10.1016/j.engfracmech.2013.02.021

Kiran R, Khandelwal K, 2014a. Experimental studies and models for ductile fracture in ASTM A992 steels at high triaxiality. *Journal of Structural Engineering*, 140(2): 04013044. https://doi.org/10.1061/(ASCE)ST.1943-541X.0000828

Kiran R, Khandelwal K, 2014b. Fast-to-compute weakly coupled ductile fracture model for structural steels. *Journal of Structural Engineering*, 140(6):04014018. https://doi.org/10.1061/(ASCE)ST.1943-541X.0001025

Kiran R, Khandelwal K, 2014c. Gurson model parameters for ductile fracture simulation in ASTM A992 steels. *Fatigue & Fracture of Engineering Materials & Structures*, 37(2): 171-183. https://doi.org/10.1111/ffe.12097

Kong DY, Yang B, 2020. Enhanced voids growth model for ductile fracture prediction of high-strength steel Q690D under monotonic tension: experiments and numerical simulation. *Journal of Structural Engineering*, 146(6): 04020107. https://doi.org/10.1061/(ASCE)ST.1943-541X.0002658

Kossakowski PG, 2012. Prediction of ductile fracture for S235JR steel using the stress modified critical strain and Gurson-Tvergaard-Needleman models. *Journal of Materials in Civil Engineering*, 24(12):1492-1500. https://doi.org/10.1061/(ASCE)MT.1943-5533.0000546

Kulawinski D, Iding K, Schornstein R, et al., 2020. Improvement of the inverse finite element analysis approach for tensile and toughness predictions by means of small punch

technique. ASME Turbo Expo: Turbomachinery Technical Conference and Exposition. https://doi.org/10.1115/GT2020-16054

Kumar P, Dutta BK, Chattopadhyay J, 2017. Fracture toughness prediction of reactor grade materials using pre-notched small punch test specimens. *Journal of Nuclear Materials*, 495:351-362. https://doi.org/10.1016/j.jnucmat.2017.08.035

Lemaitre J, 1985. A continuous damage mechanics model for ductile fracture. *Journal of Engineering Materials and Technology*, 107(1):83-89. https://doi.org/10.1115/1.3225775

Li H, Pan XF, Yuan H, 2015. A nonlocal treatment technique based on the background cell concept for micromechanical damage modeling. *Acta Mechanica*, 226(5): 1529-1547. https://doi.org/10.1007/s00707-014-1268-0

Li JC, Li SP, Xie ZY, et al., 2015. Numerical simulation of incremental sheet forming based on GTN damage model. *The International Journal of Advanced Manufacturing Technology*, 81(9):2053-2065. https://doi.org/10.1007/s00170-015-7333-6

Linse T, Kuna M, Viehrig HW, 2014. Quantification of brittle-ductile failure behavior of ferritic reactor pressure vessel steels using the small-punch-test and micromechanical damage models. *Materials Science and Engineering: A*, 614:136-147. https://doi.org/10.1016/j.msea.2014.05.095

Mahnken R, 2002. Theoretical, numerical and identification aspects of a new model class for ductile damage. *International Journal of Plasticity*, 18(7):801-831. https://doi.org/10.1016/S0749-6419(00)00105-4

Malcher L, Pires FMA, de Sá JMAC, 2014. An extended GTN model for ductile fracture under high and low stress triaxiality. *International Journal of Plasticity*, 54:193-228. https://doi.org/10.1016/j.ijplas.2013.08.015

Mansouri LZ, Chalal H, Abed-Meraim F, 2014. Ductility limit prediction using a GTN damage model coupled with localization bifurcation analysis. *Mechanics of Materials*, 76: 64-92. https://doi.org/10.1016/j.mechmat.2014.06.005

McClintock FA, 1968. A criterion for ductile fracture by the growth of holes. *Journal of Applied Mechanics*, 35(2): 363-371. https://doi.org/10.1115/1.3601204

Neimitz A, Galkiewicz J, Dzioba I, 2018. Calibration of constitutive equations under conditions of large strains and stress triaxiality. *Archives of Civil and Mechanical Engineering*, 18(4):1123-1135. https://doi.org/10.1016/j.acme.2018.02.013

Nguyen HH, Nguyen TN, Vu HC, 2018. Ductile fracture prediction and forming assessment of AA6061-T6 aluminum alloy sheets. *International Journal of Fracture*, 209(1-2): 143-162. https://doi.org/10.1007/s10704-017-0249-4

Pal S, Wathugala GW, Kundu S, 1996. Calibration of a constitutive model using genetic algorithms. *Computers and Geotechnics*, 19(4):325-348. https://doi.org/10.1016/S0266-352X(96)00006-7

Pineau A, Benzerga AA, Pardoen T, 2016. Failure of metals I: brittle and ductile fracture. *Acta Materialia*, 107:424-483. https://doi.org/10.1016/j.actamat.2015.12.034

Rice JR, Tracey DM, 1969. On the ductile enlargement of voids in triaxial stress fields. *Journal of the Mechanics and Physics of Solids*, 17(3):201-217. https://doi.org/10.1016/0022-5096(69)90033-7

Rossoll A, Berdin C, Prioul C, 2002. Determination of the fracture toughness of a low alloy steel by the instrumented Charpy impact test. *International Journal of Fracture*, 115(3):205-226. https://doi.org/10.1023/A:1016323522441

Rousselier G, 1987. Ductile fracture models and their potential in local approach of fracture. *Nuclear Engineering and Design*, 105(1):97-111. https://doi.org/10.1016/0029-5493(87)90234-2

Sajid HU, Kiran R, 2018. Influence of high stress triaxiality on mechanical strength of ASTM A36, ASTM A572 and ASTM A992 steels. *Construction and Building Materials*, 176:129-134. https://doi.org/10.1016/j.conbuildmat.2018.05.018

Seupel A, Kuna M, 2019. A gradient-enhanced damage model motivated by engineering approaches to ductile failure of steels. *International Journal of Damage Mechanics*, 28(8): 1261-1296. https://doi.org/10.1177/1056789518823879

Seupel A, Hütter G, Kuna M, 2020. On the identification and uniqueness of constitutive parameters for a non-local GTN-model. *Engineering Fracture Mechanics*, 229:106817. https://doi.org/10.1016/j.engfracmech.2019.106817

Smith C, Kanvinde A, Deierlein G, 2017. Calibration of continuum cyclic constitutive models for structural steel using particle swarm optimization. *Journal of Engineering Mechanics*, 143(5):04017012. https://doi.org/10.1061/(ASCE)EM.1943-7889.0001214

Soyarslan C, Gülçimen B, Bargmann S, et al., 2016. Modeling of fracture in small punch tests for small- and large-scale yielding conditions at various temperatures. *International Journal of Mechanical Sciences*, 106:266-285. https://doi.org/10.1016/j.ijmecsci.2015.12.007

Steglich D, Brocks W, 1998. Micromechanical modelling of damage and fracture of ductile materials. *Fatigue & Fracture of Engineering Materials & Structures*, 21(10):1175-1188. https://doi.org/10.1046/j.1460-2695.1998.00078.x

Sun GQ, Sun FY, Cao FL, et al., 2015. Numerical simulation of tension properties for Al-Cu alloy friction stir-welded joints with GTN damage model. *Journal of Materials Engineering and Performance*, 24(11):4358-4363. https://doi.org/10.1007/s11665-015-1715-7

Sun Q, Lu YB, Chen JJ, 2020. Identification of material parameters of a shear modified GTN damage model by small punch test. *International Journal of Fracture*, 222(1-2): 25-35. https://doi.org/10.1007/s10704-020-00428-4

Teng BA, Wang WN, Liu YQ, et al., 2014. Bursting prediction of hydroforming aluminium alloy tube based on

Gurson-Tvergaard-Needleman damage model. *Procedia Engineering*, 81:2211-2216. https://doi.org/10.1016/j.proeng.2014.10.310

Teng BG, Wang WN, Xu YC, 2017. Ductile fracture prediction in aluminium alloy 5A06 sheet forming based on GTN damage model. *Engineering Fracture Mechanics*, 186:242-254. https://doi.org/10.1016/j.engfracmech.2017.10.014

Tvergaard V, 1981. Influence of voids on shear band instabilities under plane strain conditions. *International Journal of Fracture*, 17(4):389-407. https://doi.org/10.1007/BF00036191

Tvergaard V, Needleman A, 1984. Analysis of the cup-cone fracture in a round tensile bar. *Acta Metallurgica*, 32(1): 157-169. https://doi.org/10.1016/0001-6160(84)90213-X

Vaz Jr M, Muñoz-Rojas PA, Cardoso EL, et al., 2016. Considerations on parameter identification and material response for Gurson-type and Lemaitre-type constitutive models. *International Journal of Mechanical Sciences*, 106:254-265. https://doi.org/10.1016/j.ijmecsci.2015.12.014

Wang LY, Li L, 2017. Parameter identification of GTN model using response surface methodology for high-strength steel BR1500HS. *Journal of Materials Engineering and Performance*, 26(8):3831-3838. https://doi.org/10.1007/s11665-017-2806-4

Wen HJ, Mahmoud H, 2016. New model for ductile fracture of metal alloys. I: monotonic loading. *Journal of Engineering Mechanics*, 142(2):04015088. https://doi.org/10.1061/(ASCE)EM.1943-7889.0001009

Yan S, Zhao XZ, 2018. A fracture criterion for fracture simulation of ductile metals based on micro-mechanisms. *Theoretical and Applied Fracture Mechanics*, 95:127-142. https://doi.org/10.1016/j.tafmec.2018.02.005

Yan S, Zhao XZ, Wu AH, 2018. Ductile fracture simulation of constructional steels based on yield-to-fracture stress–strain relationship and micromechanism-based fracture criterion. *Journal of Structural Engineering*, 144(3): 04018004. https://doi.org/10.1061/(ASCE)ST.1943-541X.0001970

Yan YX, Sun Q, Chen JJ, et al., 2013. The initiation and propagation of edge cracks of silicon steel during tandem cold rolling process based on the Gurson–Tvergaard–Needleman damage model. *Journal of Materials Processing Technology*, 213(4):598-605. https://doi.org/10.1016/j.jmatprotec.2012.11.006

Ying L, Wang DT, Liu WQ, et al., 2018. On the numerical implementation of a shear modified GTN damage model and its application to small punch test. *International Journal of Material Forming*, 11(4):527-539. https://doi.org/10.1007/s12289-017-1362-7

Yoshida F, Urabe M, Hino R, et al., 2003. Inverse approach to identification of material parameters of cyclic elastoplasticity for component layers of a bimetallic sheet. *International Journal of Plasticity*, 19(12):2149-2170. https://doi.org/10.1016/S0749-6419(03)00063-9

Yu HL, Tieu K, Lu C, et al., 2014. Tensile fracture of ultrafine grained aluminum 6061 sheets by asymmetric cryorolling for microforming. *International Journal of Damage Mechanics*, 23(8):1077-1095. https://doi.org/10.1177/1056789514538083

Yuenyong J, Suthon M, Kingklang S, et al., 2018. Formability prediction for tube hydroforming of stainless steel 304 using damage mechanics model. *Journal of Manufacturing Science and Engineering*, 140(1):011006. https://doi.org/10.1115/1.4038208

Yun GJ, Shang S, 2011. A self-optimizing inverse analysis method for estimation of cyclic elasto-plasticity model parameters. *International Journal of Plasticity*, 27(4):576-595. https://doi.org/10.1016/j.ijplas.2010.08.003

Zhang TR, Lu K, Mano A, et al., 2021. A novel method to uniquely determine the parameters in Gurson–Tvergaard–Needleman model. *Fatigue & Fracture of Engineering Materials & Structures*, 44(12):3399-3415. https://doi.org/10.1111/ffe.13568

Zhang WW, Cong S, 2016. Failure analysis of SUS304 sheet during hydro-bulging based on GTN ductile damage model. *The International Journal of Advanced Manufacturing Technology*, 86(1):427-435. https://doi.org/10.1007/s00170-015-8199-3

Zhang Y, Lorentz E, Besson J, 2018. Ductile damage modelling with locking-free regularised GTN model. *International Journal for Numerical Methods in Engineering*, 113(13):1871-1903. https://doi.org/10.1002/nme.5722

Zhao PJ, Chen ZH, Dong CF, 2016. Failure analysis based on microvoids damage model for DP600 steel on in-situ tensile tests. *Engineering Fracture Mechanics*, 154:152-168. https://doi.org/10.1016/j.engfracmech.2015.11.017

Zhong J, Xu T, Guan K, et al., 2016. Determination of ductile damage parameters using hybrid particle swarm optimization. *Experimental Mechanics*, 56(6):945-955. https://doi.org/10.1007/s11340-016-0141-6

Zhu YZ, Engelhardt MD, 2018a. A nonlocal triaxiality and shear dependent continuum damage model for finite strain elastoplasticity. *European Journal of Mechanics-A/Solids*, 71:16-33. https://doi.org/10.1016/j.euromechsol.2018.03.012

Zhu YZ, Engelhardt MD, 2018b. Prediction of ductile fracture for metal alloys using a shear modified void growth model. *Engineering Fracture Mechanics*, 190:491-513. https://doi.org/10.1016/j.engfracmech.2017.12.042